

## Article

# A CFD Modelling Approach of Fuel Spray under Initial Non-Reactive Conditions in an Optical Engine

Lis Corral-Gómez <sup>1</sup> , Francisco J. Martos <sup>2,\*</sup> , Pablo Fernández-Yáñez <sup>1</sup> and Octavio Armas <sup>1</sup> 

<sup>1</sup> Escuela de Ingeniería Industrial y Aeroespacial, Instituto de Investigación Aplicada a la Industria Aeronáutica, Campus de Excelencia Internacional en Energía y Medioambiente, Universidad de Castilla-La Mancha, Av. Carlos III, s/n, 45071 Toledo, Spain; lis.corral@uclm.es (L.C.-G.); pablo.fernandezyanez@uclm.es (P.F.-Y.); octavio.armas@uclm.es (O.A.)

<sup>2</sup> Escuela de Ingenierías Industriales, Universidad de Málaga, c/Doctor Ortiz Ramos, s/n, 29071 Málaga, Spain

\* Correspondence: fjmartos@uma.es

**Abstract:** A better understanding of why and how pollutant emissions from compression ignition engines are produced is one of the strategies to reduce them, and to achieve this it is important to understand what happens in the fuel injection inside the combustion chamber and in the combustion process. Experimentally, it is difficult to analyse the fuel spray right at the initial moments when it enters the combustion chamber due to its high velocity. These initial moments of the fuel spray affect its complete development and, consequently, the combustion process inside the chamber. This fact has motivated the approach of this work, in which a parametric study of the spray penetration as a function of variables that can be measured has been proposed. The purpose of this model is to understand which variables of the injection system significantly affect the spray penetration in the initial instants and how they affect it. This study was carried out using diesel and serves as a reference framework for similar studies using pure or blended sustainable advanced fuels. A computational fluid dynamics (CFD) model that determines the spray penetration at initial instants under different injection pressures and nozzle hole diameters is presented in this work. To tune the model, experiments were carried out on an optical engine. The modelled and experimental results exceed 94.8% agreement in all cases studied.

**Keywords:** optical engine; compression ignition engines; fuel spray; computational fluid dynamics



**Citation:** Corral-Gómez, L.; Martos, F.J.; Fernández-Yáñez, P.; Armas, O. A CFD Modelling Approach of Fuel Spray under Initial Non-Reactive Conditions in an Optical Engine. *Energies* **2023**, *16*, 6537. <https://doi.org/10.3390/en16186537>

Academic Editors: Mirko Baratta and Daniela Anna Misul

Received: 31 July 2023

Revised: 5 September 2023

Accepted: 9 September 2023

Published: 11 September 2023



**Copyright:** © 2023 by the authors. Licensee MDPI, Basel, Switzerland. This article is an open access article distributed under the terms and conditions of the Creative Commons Attribution (CC BY) license (<https://creativecommons.org/licenses/by/4.0/>).

## 1. Introduction

For years, there has been great concern about the consequences of exhaust emissions from internal combustion engines on the environment and on people's health [1,2]. Compression ignition engines or diesel engines have high thermal efficiency but produce high soot, nitrogen oxides, hydrocarbons and particulate matter emissions [3,4]. Many strategies have been used to reduce these emissions over the years, such as engine modifications, new advanced combustion technologies or the use of renewable fuels, but to better understand why and how these emissions are produced, it is important to understand what happens in the fuel injection inside the combustion chamber and combustion process [5–8].

One of the parameters that contributes to the formation of emissions is the flame lift-off length. This parameter is defined as the distance that exists between the tip of the injector and the closest location of the spray combustion that takes place after the autoignition phase of the injected fuel. Most of the fuel within the flame lift-off length is in the liquid phase [9,10]. Thus, to some extent, the flame lift-off length is related to the liquid phase length [11,12], since the liquid phase reaches its maximum penetration shortly after the start of the injection, while the vapour phase continues to penetrate [13]. A proper lift-off length can help the air entrainment of the spray so the engine has a better combustion and generates less soot and hydrocarbon emissions [14–16]. Reducing the nozzle orifice

diameter and increasing the injection pressure have been important decisions to facilitate fuel–ambient gas blending formation and its subsequent combustion in diesel engines [17].

Hespel et al. [18] studied the evolution of the liquid penetration with the variation of the gas temperature in the combustion chamber for three different nozzles, this dependence being inversely proportional. They also observed that liquid length decreases with increasing gas pressure inside the combustion chamber. They concluded that liquid length decreased due to the decrease of the molecular weight and the increase of the thermal conductivity of the gas inside the combustion chamber.

To understand the effects of different factors on liquid length, Naber and Siebers [19] developed a one-dimensional model in which they deduced that vaporisation depends more on air entrainment than on interphase transport. Some correlations have been proposed relating macroscopic parameters of the fuel spray to injection system variables, such as injection pressure and nozzle orifice diameter, as well as to combustion chamber variables [20,21]. Payri et al. [22] studied these same variables on fuel spray at the initial moments of fuel entry into the combustion chamber.

Depending on the assumptions considered, there are different models proposed in the literature to characterise the fuel spray inside the combustion chamber. Xu et al. [23] proposed a one-dimensional model of the fuel spray and compared it with a CFD model. García-Oliver et al. [24] combined 1D and 3D models in CFD to optimise the computational power required. Desantes et al. [25] proposed a combined phenomenological and CFD model to characterise diesel spray under evaporative conditions. Other work focused on studying the flame lift-off length using CFD models [26,27], while others studied the fuel spray under reactive conditions [28]. But there are few studies of fuel spray under non-reactive but evaporative conditions [29].

Experimentally, it is difficult to analyse the fuel spray right at the initial moments when it enters the combustion chamber, due to its high velocity. This fact has motivated the approach of this work, in which a parametric study of the spray penetration has been proposed as a function of variables that can be measured. The purpose of this model is to understand and be able to reproduce in a model which variables of the injection system significantly affect the spray penetration in the initial instants and how they affect it. This study was carried out using diesel and serves as a reference framework for similar studies using pure or blended sustainable advanced fuels. A computational fluid dynamics model that determines the spray penetration at initial moments under different injection pressures and nozzle hole diameters is presented in this work. The experiments were carried out on an optically accessible motor. The modelled and experimental results exceed 94.8% agreement in all cases studied.

In addition to the introduction, Section 2 describes the experimental facility and methodology, Section 3 explains the description of the model, Section 4 shows and discusses the experimental and model results obtained and Section 5 presents the main conclusions of this work.

## 2. Experimental Facility and Methodology

Experimental tests were carried out on a single-cylinder two-stroke diesel engine (Jenbacher JW-50), which is explained in detail in [30]. It has an effective compression ratio of 9.5 and a displacement of 3 L. The experimental facility is optically accessible as it has four accesses on each side of the cylinder head. An in-cylinder pressure sensor was installed in one of the four side accesses, while three oval-shaped quartz windows (L88xW37xE28, R18) were installed in the other three.

The engine was driven by an asynchronous electric motor that allowed it to start from rest up to the desired speed of 500 rpm ( $\text{min}^{-1}$ ) as well as to maintain it at a constant speed during the tests. An external and independent lubrication-cooling system was responsible for establishing the temperature of the coolant and the lube oil of the engine at 60 °C. The intake air pressure was raised to 1.3 bar (0.13 MPa) using a Roots compressor and the intake air temperature was conditioned to 50 °C with five heaters installed in the inlet

line. An injection was performed every 64 engine cycles in order to reduce the thermal and mechanical stresses of the quartz windows. The experimental facility allowed working in reactive atmosphere and in inert atmosphere. For these experimental tests, the reactive atmosphere was used.

The experimental installation had a Bosch common-rail system, which was equipped with three different solenoid fuel injectors, with hole diameters of 115  $\mu\text{m}$ , 130  $\mu\text{m}$  and 150  $\mu\text{m}$ . Each injector had a single-hole axial nozzle with a K-factor of 3.5. The parameters of injector energization time, start of injection, fuel temperature and injection pressure were commanded and modified from the control system of the experimental facility.

Figure 1 shows the diagram of the visualization system used in the experimental setup. It consists of the Schlieren optical technique which makes it possible to observe the variation of the density gradients of a transparent and inhomogeneous medium [31]. This technique allows to study of macroscopic parameters of fuel spraying, such as spray penetration, cone angle and area [32].

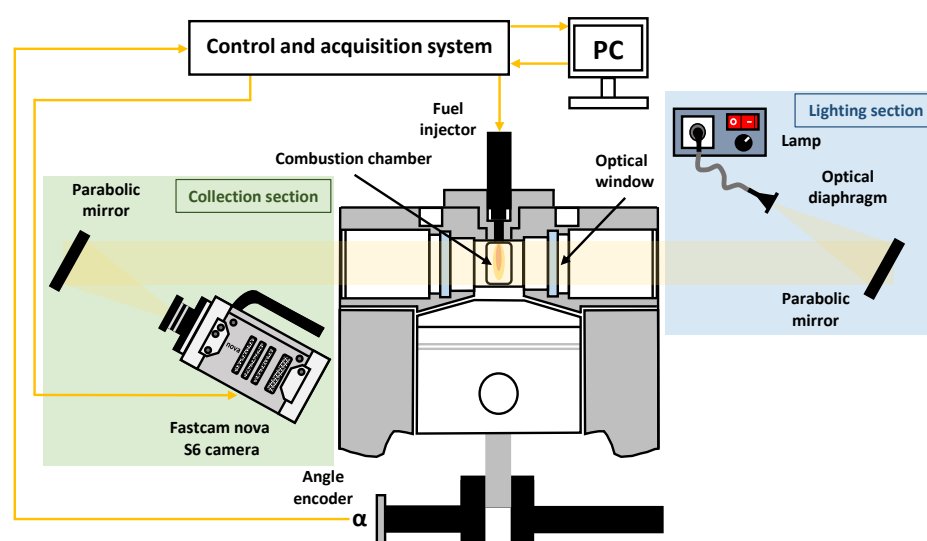


**Figure 1.** Schematic diagram of the Schlieren system used in experimental facility.

The Schlieren optical technique is composed of a light source and two parabolic mirrors that form a light path through the cylinder head. The parabolic mirrors are each placed on the sides of the cylinder head at a focal length of  $f = 1000$  mm and the light source is obtained with a focusing lens of  $f = 50.3$  mm and a 150 W lamp. A high-speed camera (Fastcam nova S6) is responsible for capturing the images focused by one of the parabolic mirrors. The frame rate used is 15,000 frames per second (FPS), the resolution of the images is  $896 \times 512$  pixels and the approximate ratio between world and image units is 10.5 pixels/mm. The control software is in charge of synchronously sending the trigger signal of the high-speed camera and the activation of the injector to obtain the images of the spray. Five repetitions are made for each experimental test, and in each repetition 10 images are taken before the trigger signal and 90 images after it. The penetration length of the experimental spray was measured from the binarisation of the calibrated photographs obtained with the high-speed camera. The complete procedure is explained in Corral-Gómez et al. [33].

Regarding the fuel, an ultralow-sulphur diesel fuel without biodiesel, supplied by REPSOL, was used as reference fuel. The main physical–chemical properties of the fuel are shown in Table 1.

The understanding of the dependence between non-reactive spray penetration, injection pressure and nozzle hole diameter has been improved due to experimental tests. In addition, experimental data have been used to validate the proposed model. A correla-

tion to determine the initial non-reactive spray penetration as a function of some variables of the injection system has been proposed based on the results of all simulations.

**Table 1.** Main physico-chemical properties of the fuel tested.

Properties	Value	Properties	Value
C (% w/w)	86.2	H (% w/w)	13.8
Viscosity at 40 °C (cSt)	2.96	Cetane number	54.5
HHV (MJ/kg)	45.97	LHV (MJ/kg)	43.18
CFPP (°C)	−19	Flash point (°C)	61
Density at 15 °C (kg/m <sup>3</sup> )	835.8	Density at 40 °C (kg/m <sup>3</sup> )	827.6
Distillation (vol.):			
10% (°C)	206.5	50% (°C)	275.9
90% (°C)	344.9		

### 3. Model Description

#### 3.1. Optical Engine Model

Figure 2a shows an actual image of the combustion chamber of the optical engine. The outer section is quadrangular and has a transparent window on each face where the spray formation can be visualised. Figure 2b shows the 3D model of the combustion chamber made in SolidWorks® 2021 SP4.0. Figure 2c,d show the axial and cross sections, respectively, of the combustion chamber. The injector has a single hole centred on the vertical axis of the combustion chamber. This made it possible to produce a 2D axisymmetric model, with the consequent computational savings.

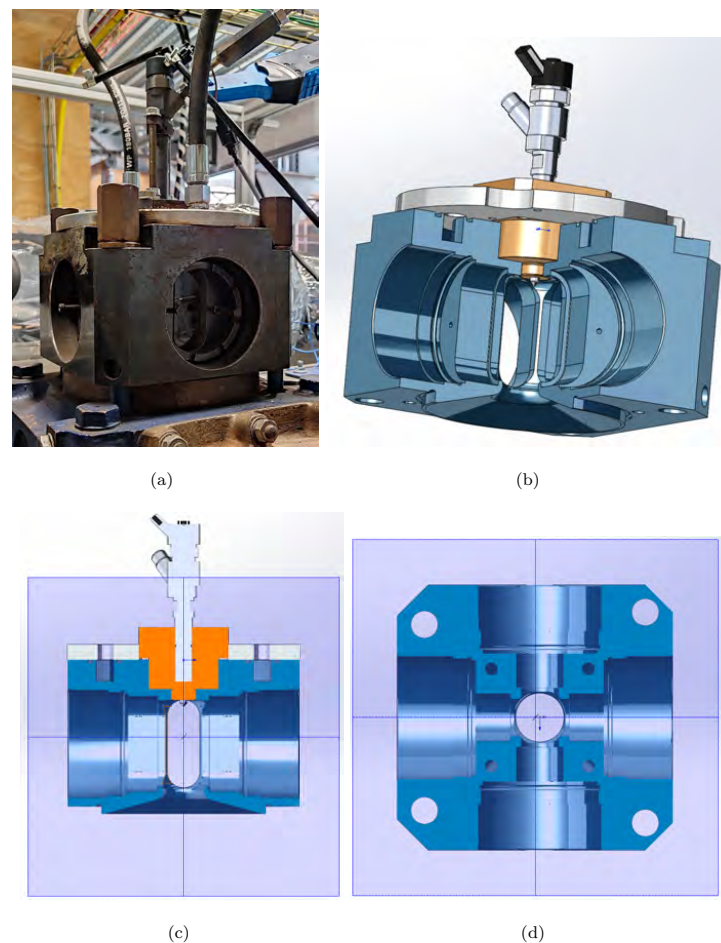


**Figure 2.** Physical model of the optical engine. (a) Engine tested, (b) 3D model, (c) axial section and (d) cross-section.

The 2D axisymmetric model was made in Ansys® SpaceClaim® 2021 R2. Hydrodynamic and thermal boundary layers were considered in the meshing. For the maximum  $y^+$  in the whole domain to be less than 5, the inflation technique was used. Thus, the viscous effects within the boundary layer are close to reality [34]. The meshing was performed with 360,000 four-node rectangles (Quad4). To obtain this value, a mesh convergence study was carried out. An orthogonal mesh quality close to one was obtained. The boundary conditions, discretisation scheme, solution method, convergence criteria and computers used are explained in [35].

Thirteen nozzle hole diameters have been simulated, ranging from 90  $\mu\text{m}$  to 200  $\mu\text{m}$  in 10  $\mu\text{m}$  steps, including the experimental nozzle hole diameter of 115  $\mu\text{m}$ , and seventeen injection pressures, ranging from 400 bar to 2000 bar in 100 bar steps. Therefore, a total of  $17 \times 13 = 221$  simulations have been carried out. The simulations were performed in Ansys® Fluent® 2021 R2 and the meshing in Ansys® Meshing® 2021 R2.

The minimum and maximum fuel mass flow rates at the nozzle hole outlet are 1.5 and 11 g/s for nozzle hole diameters of 90 and 200  $\mu\text{m}$ , respectively. The average fuel temperature is between 40 °C and 200 °C, so the kinematic viscosity is between 2.96 cSt and 0.038 cSt, respectively. The calculated Reynolds number is in the range 8700 and  $2.69 \times 10^6$ , so the flow is predominantly turbulent. The turbulence model used is justified and explained in [35,36].

### 3.2. Fluid Model

Antoine's law, Equation (1), was used to determine the local partial vapour pressure,  $p_v$  in (Pa), as a function of the phase change temperature of the fuel,  $T$  in (K).

$$\ln p_v = A - \frac{B}{T + C} \quad (1)$$

where, for diesel fuel, the constants  $A = 18.9970$ ,  $B = 3526.20$  and  $C = -43.7896$  were taken from [37]. The local fuel density,  $\rho$  in ( $\text{kg}/\text{m}^3$ ), was modelled with the Tait equation:

$$\rho = \rho_0 \left( 1 + \frac{n(p - 0.1013)}{K} \right)^{\frac{1}{n}} \quad (2)$$

where  $\rho_0$  is the temperature-dependent local density of the fuel at ambient pressure,  $\rho_0 = 1061.5 - 0.7471 \cdot T$  [38].  $K$  is the local compressibility module of the fuel,  $K = 3748.7 - 7.127 \cdot T$  [38]. In both expressions,  $T$  is in (K). From Cristofaro et al. [39], the exponent and factor  $n = 7$  has been taken.

The local dynamic viscosity of the fuel,  $\mu$  in ( $\text{mPa}\cdot\text{s}$ ), was calculated with the Equations (3) and (4). Both correlations were published in [40].

$$\mu = \mu_0 \cdot 10^{(-1.48 + 5.86\mu_0^{0.181}) \left( \frac{p - 0.1013}{1000} \right)} \quad (3)$$

$$\mu_0 = 3.7456 \cdot \exp[-0.0283(T - 298)] \quad (4)$$

In Equations (2) and (3),  $p$  is the local pressure in (MPa). In the Equation (4) the multiplying factor has been modified to obtain the fuel viscosity at 40 °C (Table 1). In Equation (4),  $T$  is the local temperature in (K).

The density and viscosity of the air were calculated with the Redlich–Kwong equation and the Sutherland equation, respectively.

### 3.3. Spray Model

Transport of non-reacting species within the combustion chamber has been taken into account. The species diffusion flux at the inlet, the diffusion energy source and the thermal diffusion were considered. In the energy equation, the effect of enthalpy transport due to species diffusion was also taken into account.

The liquid droplets formed after the nozzle were modelled as a discrete phase. The interaction of the discrete phase with the continuous phase formed by the mixture of air and diesel vapour was considered. Away from the injector tip, where the droplets form a dispersed phase suspended in the gas, the droplet trajectories were determined using the Lagrangian approach, including the effect of inertia and hydrodynamic drag. The effects of droplet distortion were considered in the dynamic drag. The simulation was performed using transient flow in which the Courant number was always less than five.

The turbulent dispersion of the discrete phase was performed using a discrete random walk model and random eddy lifetime. The effect of the instantaneous turbulent velocity formulations was taken into account in the particle trajectories using the stochastic method.

Vaporisation and boiling of diesel liquid droplets in diesel vapour were considered in the spray model. The probability of high vaporisation rates is high, so in addition to diffusive flow, the effect of convective flow from the droplet surface to the gas phase was taken into account. The vaporisation rate, Equation (5), has been obtained from Miller et al. [41] and Sazhin [42].

$$\frac{dm_d}{dt} = \rho_d k_c A_d \ln(1 + B_m) \quad (5)$$

where  $m_d$  is the droplet mass,  $\rho_d$  is the liquid fuel density,  $A_d$  is the droplet surface area,  $k_c$  is the mass transfer coefficient and  $B_m$  is the Spalding mass number which is determined by Equation (6).

$$B_m = \frac{Y_s - Y_\infty}{1 - Y_s} \quad (6)$$

where  $Y_s$  is the vapour mass fraction at the surface and  $Y_\infty$  is the vapour mass fraction in the bulk gas.  $k_c$  is determined from Sherwood number,  $Sh$ , with the correlation shown in Equation (7), obtained from Ranz [43].

$$Sh = \frac{k_c d_d}{D_m} = 2.0 + 0.6 Re_d^{1/2} Sc^{1/3} \quad (7)$$

where  $d_d$  is the droplet diameter,  $D_m$  is the mass diffusion coefficient of vapour in the bulk gas,  $Re_d$  is the Reynolds number and  $Sc$  is the Schmidt number.

In the spray model, coalescence and stochastic collision of droplets were taken into account. The O'Rourke's algorithm [44] has been used to model stochastic collisions. This algorithm performs a stochastic estimation of collisions, rather than analysing whether the parcel trajectories cross, and further assumes that two parcels can collide if they are in the same cell. The head-on collision of two droplets ends in coalescence, while the oblique collision ends in rebound. The probability of coalescence is related to the distance between the centre of the larger droplet and the trajectory of the smaller droplet. According to [44], the critical distance to decide between coalescence and rebound is a function of the collisional Weber number and the radii of the two droplets.

Due to the high values of Weber numbers and pressures, the Kelvin–Helmholtz/Rayleigh–Taylor (KH-RT) model was used to simulate the droplet breakup. The effects of Kelvin–Helmholtz waves driven by aerodynamic forces and Rayleigh–Taylor instabilities due to droplet acceleration are considered.

In the wave model (KH model), the radius of the newly-formed droplets,  $r_n$ , is assumed to be proportional to the wavelength,  $\Lambda_w$ , of the fastest growing unstable surface wave, i.e.,  $r_n = B_0 \Lambda_w$  [45]. This wave is created on the surface of the cylindrical liquid jet with initial radius,  $r_p$ . From Reitz [46], the value of the proportionality constant,  $B_0$ , equal to 0.61 has been taken. The rate of change of parent droplet radius is shown in Equation (8) [47].

$$\frac{dr_p}{dt} = -\frac{(r_p - r_n)}{\tau}, r_n \leq r_p \quad (8)$$

where  $\tau$  is the breakup time calculated from Equation (9).

$$\tau = \frac{3.726B_1r_p}{\Lambda_w\Omega_w} \quad (9)$$

where  $\Omega_w$  is the maximum growth rate. From Reitz [46],  $\Omega_w$  and  $\Lambda_w$  are determined as a function of the Ohnesorge number, Taylor number and Weber numbers of the liquid and gas.  $B_1$  is the breakup time constant and as recommended by Liu et al. [48] it is set to 1.73.

The Rayleigh–Taylor (RT) model is based on the instability of waves on the droplet surface due to deceleration. Droplet breakup occurs when RT waves have been growing for longer than the breakup time,  $\tau_{RT}$ . The breakup time can be considered proportional to the inverse of the frequency of the fastest growing wave,  $\Omega_{RT}$ , i.e.,  $\tau_{RT} = C_\tau/\Omega_{RT}$ .  $C_\tau$  is the RT breakup time constant. From Beale et al. [49] and Patterson et al. [50],  $\Omega_{RT}$  is calculated by Equation (10).

$$\Omega_{RT} = \sqrt{\frac{2(a(\rho_d - \rho_g))^{3/2}}{3\sqrt{3}\sigma(\rho_d + \rho_g)}} \quad (10)$$

where  $a$  is the droplet acceleration in the direction of the droplet travel,  $\rho_d$  is the droplet density,  $\rho_g$  is the gas density and  $\sigma$  is the droplet surface tension. The corresponding wavelength,  $\Lambda_{RT}$ , is determined by Equation (11), [45].

$$\Lambda_{RT} = 2\pi C_{RT} \sqrt{\frac{3\sigma}{a(\rho_d - \rho_g)}} \quad (11)$$

where  $C_{RT}$  is the breakup radius constant. It can be deduced that the radius of the smaller child droplets is half the corresponding wavelength.  $C_{RT}$  and  $C_\tau$  depends on the geometry of the nozzle. When the nozzle is round-edged,  $C_{RT}$  and  $C_\tau$  are both unity, while if the nozzle is sharp-edged, they take the values of 0.2 and 0.4, respectively [47]. In this case, intermediate values have been chosen.

## 4. Results and Discussion

### 4.1. Test Results

The optical engine was tested with three injectors with different nozzle hole diameters. From smallest to largest, the nozzle hole diameters, together with the colour or symbol used in this work, are 115  $\mu\text{m}$  (magenta or circle), 130  $\mu\text{m}$  (brown or square) and 150  $\mu\text{m}$  (orange or diamond). In addition, for each injector, the engine was tested at four injection pressures, which were 500 bar (green), 700 bar (blue), 900 bar (red) and 1100 bar (cyan). The colour used to refer to the injection pressures tested has been indicated. The fuel and engine intake air temperatures were 40 °C and 50 °C, respectively. The start of injection (SoI) into the combustion chamber starts at  $-0.6$  degrees from top dead centre (TDC), where the average instantaneous pressure inside the combustion chamber is 29.14 bar.

Figure 3 shows the instantaneous mass flow rate for the twelve tested combinations of nozzle hole diameters and injection pressures for an injector energisation time of 1 ms.

Figure 4 shows the average mass flow rate of all tests and their 95% confidence intervals. From Figures 3 and 4a it can be seen, keeping the nozzle hole diameter constant, that the rate of change of mass flow rate decreases with increasing pressure. This effect is probably due to increased cavitation as a consequence of increased fluid flow velocities [36]. On the other hand, an increase in nozzle hole diameter with constant injection pressure leads to a linear mass flow rate behaviour, as shown in Figure 4b, when a non-linear dependence is expected. This effect can probably be due to the occurrence of cavitation as a consequence of high flow velocities in the smaller diameter nozzle holes, thus reducing the mass flow rate.

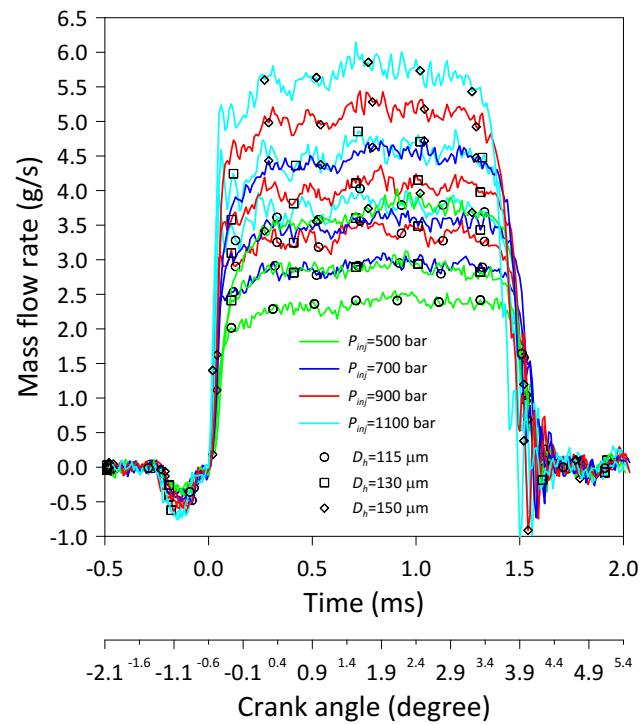


Figure 3. Injected fuel mass flow rate vs. time and crank angle.

From the mass flow rate,  $\dot{m}$ , and the difference in injection pressure,  $p_{inj}$ , and combustion chamber pressure,  $p_{ch}$ , the discharge coefficient,  $c_d^*$ , has been determined, as shown in Equation (12).

$$c_d^* = \frac{\dot{m}}{A_h \sqrt{2 \rho_f (p_{inj} - p_{ch})}} \tag{12}$$

where  $A_h$  is the cross-sectional area of the nozzle hole and  $\rho_f$  is the fuel density.

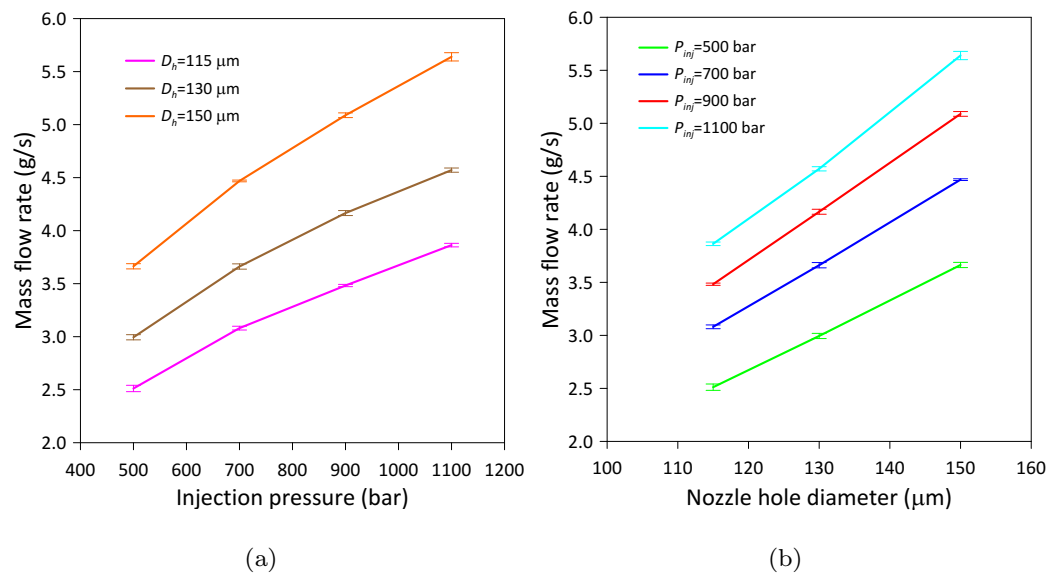
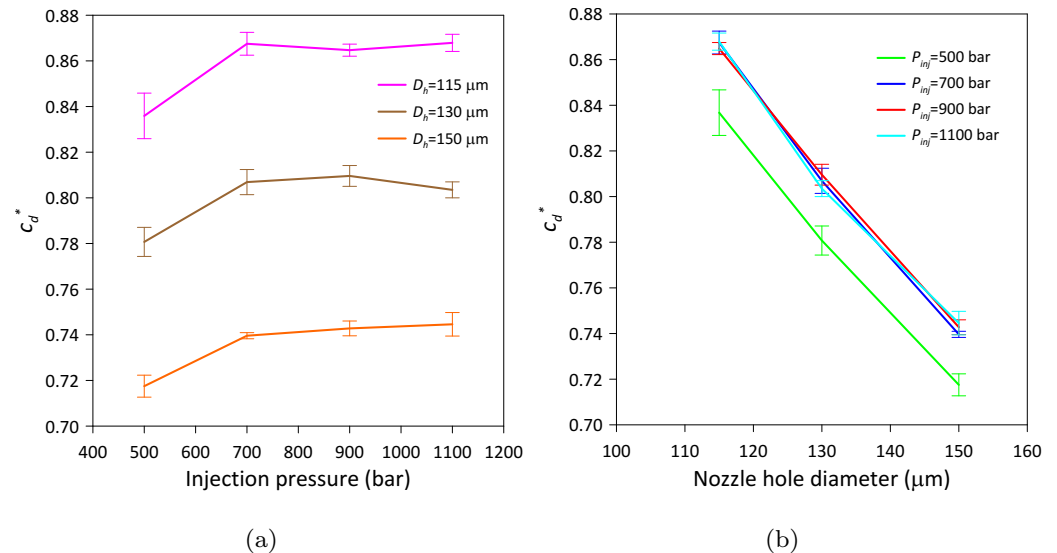


Figure 4. Average fuel mass flow rate vs. (a) injection pressure, (b) nozzle hole diameter.

Irrespective of the nozzle hole diameter, at low injection pressures the average discharge coefficient is lower than at medium and high injection pressures; see Figure 5a.

Furthermore, at medium and high pressures the average discharge coefficient remains almost constant, so the effect of the decrease in mass flow rate as a consequence of the likely occurrence of cavitation is more significant on the discharge coefficient than the increase in fluid velocity as an effect of the increase in pressure difference [36].



**Figure 5.** Average discharge coefficient vs. (a) injection pressure, (b) nozzle hole diameter.

Keeping the injection pressure constant, an increase in nozzle hole diameter implies a decrease in the average discharge coefficient, Figure 5b, so the effect of the mass flow rate on the discharge coefficient is more significant than the nozzle hole diameter. As nozzle hole diameter increases, the mass flow rate increases but at a lower rate than the nozzle hole diameter, probably due to friction, and therefore lowers the average discharge coefficient [36]. From the experimental data in Figure 5, the correlation shown in Equation (13) has been obtained, with a correlation coefficient of  $R^2 = 0.9786$ .

$$c_d^* = 1.227 - 3.424 D_h + 3.759 \cdot 10^{-5} p_{inj} \quad (13)$$

where  $D_h$  is the nozzle hole diameter in mm and  $p_{inj}$  is the injection pressure in bar. From a strict point of view, the application domains of Equation (13) would be for  $D_h$  from 115 to 150  $\mu\text{m}$  and for  $p_{inj}$  from 500 to 1100 bar. But considering the high correlation coefficient obtained and the stability and continuity of the results shown in Figure 5, Equation (13) was used for the whole simulation domain.

In all simulations proposed in Section 3.1, the mass flow rate calculated with Equation (12) has been used, where the discharge coefficient has been replaced by the one obtained with Equation (13).

For all three nozzle hole diameters, the non-reactive spray penetration increases proportionally with injection pressure, as shown in Figure 6a. The slope on a logarithmic scale is between 0.26 for the 115  $\mu\text{m}$  nozzle hole diameter and 0.37 for the 150  $\mu\text{m}$  nozzle hole diameter. These slopes are close to the value of 0.25 published in [51]. The non-reactive spray penetration, irrespective of the injection pressure, for the 130  $\mu\text{m}$  nozzle hole diameter is always slightly lower than for the other two nozzles holes, as shown in Figure 6b, although in general terms the trend of the non-reactive spray penetration is increasing with increasing nozzle hole diameter [27].

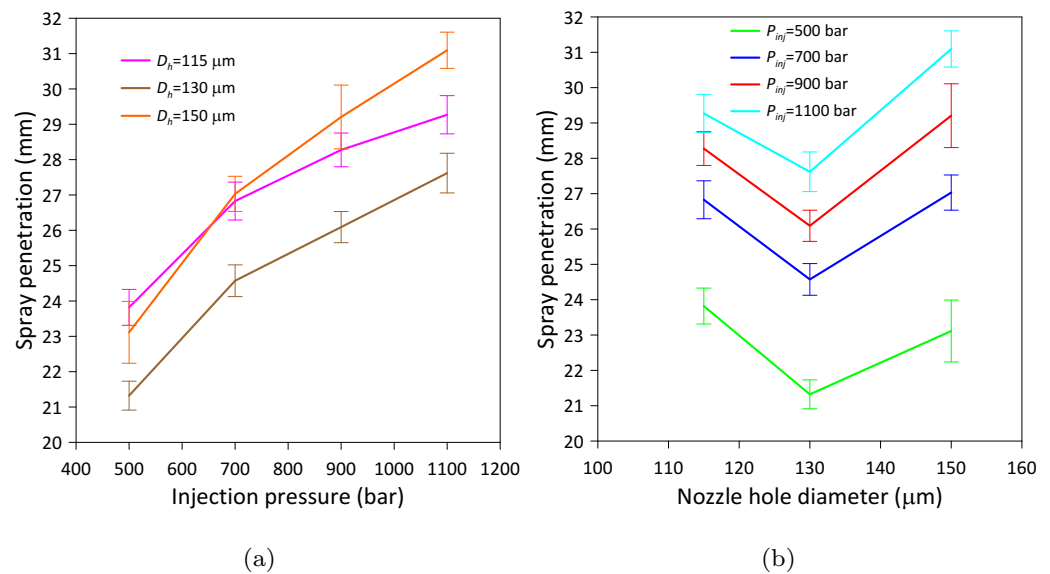


**Figure 6.** Average non-reactive spray penetration at 0.2 ms vs. (a) injection pressure, (b) nozzle hole diameter.

#### 4.2. Model Results

As an example, the experimental spray images shown in Figure 7 correspond to a nozzle hole diameter of 130  $\mu\text{m}$  and an injection pressure of 700 bar. Figure 7 shows images of the spray at three different times with respect to the instant when the spray started to enter the combustion chamber. Figure 7a corresponds to 0.0667 ms, Figure 7b to 0.1333 ms and Figure 7c to 0.2 ms. It can be seen how the growth rate of the spray penetration in the combustion chamber decreases with time [52].

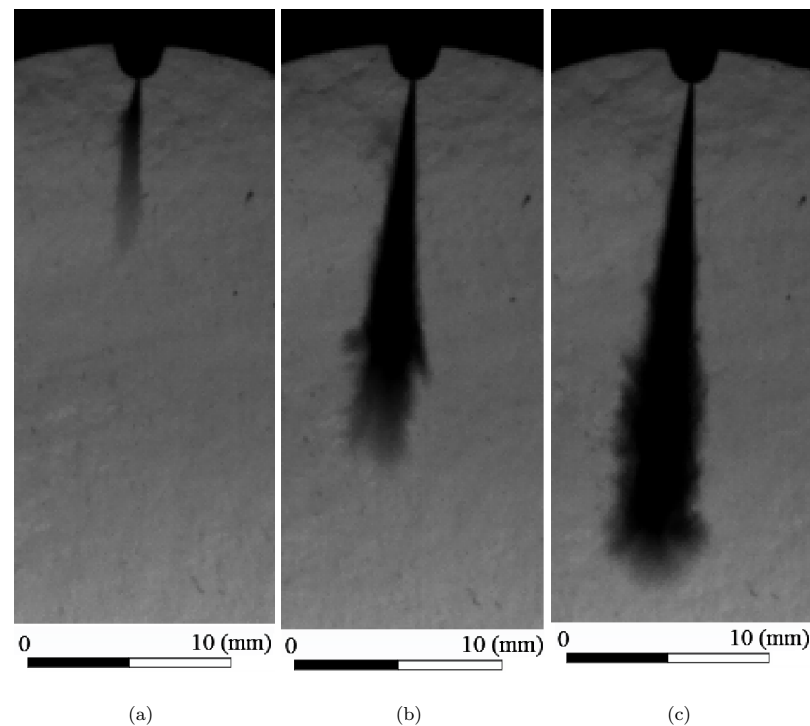


**Figure 7.** Experimental spray image at (a) 0.0667 ms, (b) 0.1333 ms and (c) 0.2 ms.

The images of the modelled spray shown in Figure 8 correspond to the same conditions as those of the experimental spray in Figure 7. These conditions are a nozzle hole diameter of 130  $\mu\text{m}$  and an injection pressure of 700 bar. Moreover, the snapshot times are the same.

Figure 8a corresponds to 0.0667 ms, Figure 8b to 0.1333 ms and Figure 8c to 0.2 ms. Figure 8 shows how the growth rate of spray penetration into the combustion chamber is of the same order as shown in Figure 7. Furthermore, the shape of the spray obtained by modelling resembles the shape of the experimental spray.

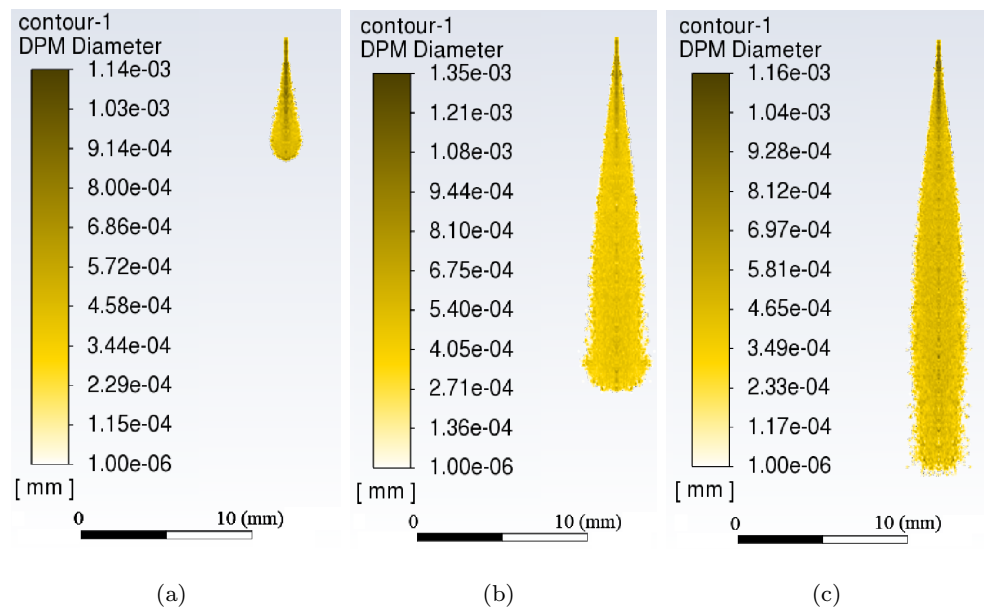


**Figure 8.** Image of the non-reactive spray modelled at (a) 0.0667 ms, (b) 0.1333 ms and (c) 0.2 ms.

As discussed in Section 3.1, a total of 221 simulations have been carried out, with the following combinations: nozzle hole diameter equal to {90, 100, 110, 115, 120, 130, 140, 150, 160, 170, 180, 190, 200} ( $\mu\text{m}$ ) and injection pressure equal to {400, 500, 600, 700, 800, 900, 1000, 1100, 1200, 1300, 1400, 1500, 1600, 1700, 1800, 1900, 2000} (bar). In some of the modelled combinations, for example at very high pressures, cavitation is likely to appear in the nozzle, causing the spray formation to be non-axisymmetric [36]. In these combinations, the results obtained must be understood as a first approximation. It is therefore necessary to extend this model to a full 3D model including the nozzle and combustion chamber assembly. Figure 9a shows the results of all simulations.

In Figure 9a, the colour map represents the non-reactive spray penetration under different conditions. Contour lines of constant non-reactive spray penetration are shown. Keeping the injection pressure constant and varying the nozzle hole diameter and vice versa, it is observed that the growth rate of the non-reactive spray penetration is similar for both cases. Moreover, in both situations, the non-reactive spray penetration is proportional to the variable being changed. This result is similar to that published in [51], although for these authors the nozzle hole diameter proportionally affects the spray penetration more than the difference between injection pressure and combustion chamber pressure.

By varying the nozzle hole diameter and the injection pressure while keeping the pressure inside the combustion chamber constant, as in this case, both the mass flow rate and the flow velocity at the nozzle hole outlet vary. Keeping the nozzle hole diameter constant and increasing the injection pressure, as shown in Figure 9a, the non-reactive spray penetration increases. This effect is due to the fact that it increases both the mass flow rate and the flow velocity at the nozzle hole outlet. On the other hand, keeping the injection pressure constant and increasing the nozzle hole diameter, as shown in Figure 9a, the non-reactive spray penetration increases as well. At low injection pressures, the increase in non-reactive spray penetration is smoother than at high injection pressures. In this case, the mass flow rate increases while the flow velocity at the nozzle hole outlet decreases, so the mass flow rate affects the spray behaviour more than the flow velocity.

Figure 9a shows with red circles the experimental measurements obtained under the twelve tested conditions.

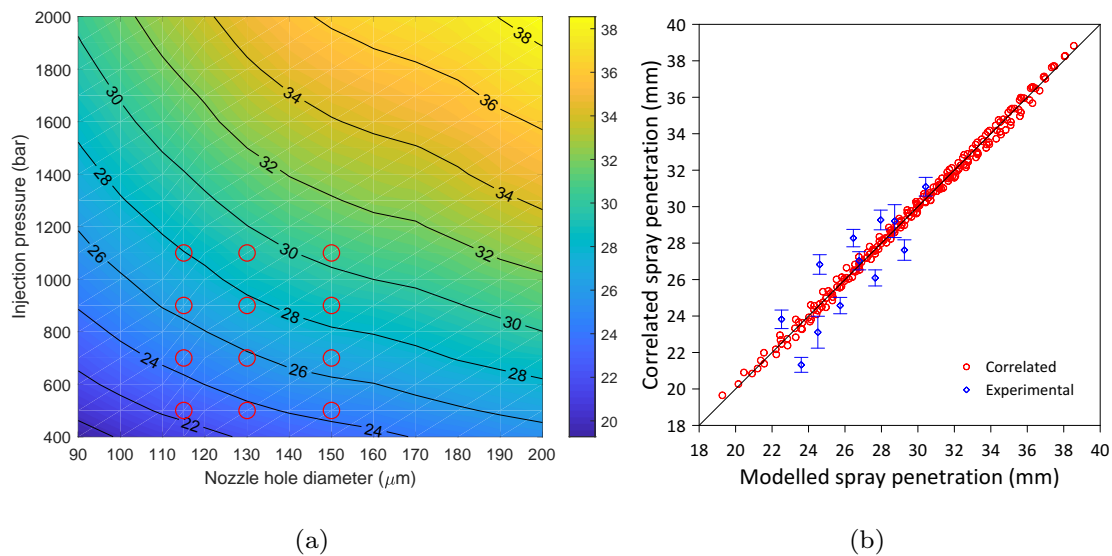


**Figure 9.** (a) Modelled and experimental (red circles) non-reactive spray penetration (mm) at 0.2 ms vs. nozzle hole diameter and injection pressure. (b) Correlated and experimental non-reactive spray penetration (mm) at 0.2 ms vs. modelled non-reactive spray penetration (mm) at 0.2 ms.

Based on the results of the simulations, a potential correlation between the three variables is proposed in Equation (14). The result of this correlation is the non-reactive spray penetration at 0.2 ms, with  $P$  in (mm). A correlation coefficient and a mean squared error of  $R^2 = 0.996$  and  $0.27$ , respectively, were obtained.

$$P = 0.9944 D_h^{0.294} p_{inj}^{0.2772} \quad (14)$$

where  $D_h$  is the nozzle hole diameter in  $\mu\text{m}$  and  $p_{inj}$  is the injection pressure in bar.  $D_h$  can take values from 90 to 200  $\mu\text{m}$  and  $p_{inj}$  from 400 to 2000 bar.

Figure 9b shows in red circles the goodness of fit of the correlation of Equation (14) and the results of all simulations. Figure 9b also shows in blue diamonds the experimental measurements with the error bars indicating the 95% confidence index. Considering the good fit achieved with the correlation of Equation (14) and the simplicity of this equation, it can be considered as a pre-calculation for the design of test matrices and as a quick calculation of the non-reactive spray penetration.

## 5. Conclusions

The non-reactive spray penetration in a combustion chamber of a compression ignition engine was analysed experimentally and with simulations with different injection pressures and nozzle hole diameters. The main conclusions of this research are:

- Keeping the nozzle hole diameter constant, the rate of change of the mass flow rate decreases with increasing injection pressure. This effect is probably due to increased cavitation as a result of increased fluid flow velocities. On the other hand, an increase in nozzle hole diameter with constant injection pressure leads to a linear mass flow rate behaviour, when a non-linear dependence is expected. This effect can probably be due to the occurrence of cavitation as a consequence of high flow velocities in the smaller diameter nozzle holes, thus reducing the mass flow rate.
- At medium and high injection pressures, the average discharge coefficient remains almost constant, so the effect of the decrease in mass flow rate as a consequence of the likely occurrence of cavitation is more significant on the discharge coefficient than the increase in fluid velocity as an effect of the increase in injection pressure difference.

Keeping the injection pressure constant, an increase in nozzle hole diameter implies a decrease in the average discharge coefficient, so the effect of the mass flow rate on the discharge coefficient is more significant than the nozzle hole diameter.

- A CFD model has been proposed. With this model, the spray penetration was simulated under non-reactive conditions under different injection pressures and nozzle hole diameters. In all cases studied, the modelled and experimental results exceed 94.8% agreement.
- The developed model has allowed us to propose a correlation to estimate the non-reactive spray penetration from easily measurable quantities on an experimental facility, such as injection pressure and nozzle hole diameter.
- The improvement of the presented model to a non-axisymmetric 3D model, including the nozzle and combustion chamber together and the extension of the testing of the experimental facility, are the planned future investigations.

**Author Contributions:** Conceptualization, O.A. and F.J.M.; methodology, O.A., L.C.-G., F.J.M. and P.F.-Y.; formal analysis, F.J.M., P.F.-Y. and O.A.; investigation, L.C.-G. and F.J.M.; resources, O.A. and F.J.M.; data curation, L.C.-G. and F.J.M.; writing—review and editing, O.A., F.J.M., L.C.-G. and P.F.-Y.; supervision, project administration and funding acquisition, O.A. All authors have read and agreed to the published version of the manuscript.

**Funding:** The authors wish to thank the financial support provided by: (i) the government of Castilla-La Mancha community to the project ASUAV, Ref. SBPLY/19/180501/000116; (ii) the Spanish Ministry of Science and Innovation to the project LOOK-AHEAD, Ref. PID2020-118387RB-C32 for the financial support to Flor de Lis Larami Corral-Gómez; and (iii) the financial support received from FEDER funds through the University of Castilla-La Mancha for the acquisition of the Schlieren equipment.

**Data Availability Statement:** Not applicable.

**Acknowledgments:** The authors wish to thank the technical support provided by: (i) the CMT-Motores Térmicos Institute for the cession of the main experimental installation (optical engine and auxiliary systems), (ii) REPSOL Technology Laboratory and SASOL Co. for supplied fuels.

**Conflicts of Interest:** The authors declare no conflict of interest.

## Abbreviations

$a$	acceleration
$A$	area
$A_h$	nozzle hole cross-sectional area
$C_d^*$	discharge coefficient
$B_m$	Spalding mass number
$d$	diameter
$D_h$	nozzle hole diameter
$D_m$	mass diffusion coefficient
$k_c$	mass transfer coefficient
$K$	fuel compressibility module
$m$	mass
$\dot{m}$	mass flow rate
$p$	pressure
$P$	non-reactive spray penetration
$r$	radius
$Re$	Reynolds number
$Sc$	Schmidt number
$Sh$	Sherwood number
$T$	temperature
$Y$	vapour mass fraction
$\Lambda$	wavelength

$\mu$	dynamic viscosity
$\Omega$	maximum growth rate
$\rho$	density
$\sigma$	droplet surface tension
$\tau$	breakup time
Subscripts	
0	ambient conditions
ch	combustion chamber
d	droplet
f	fuel
g	gas
inj	injection
n	new
p	parent
RT	RT model
s	surface
v	vapour
w	KH model
$\infty$	bulk gas
Acronyms	
CFD	Computational Fluid Dynamics
CFPP	Cold Filter Plugging Point
FPS	Frames per Second
HHV	High Heating Value
KH-RT	Kelvin–Helmholtz/Rayleigh–Taylor
LHV	Low Heating Value
SoI	Start of Injection
TDC	Top Dead Centre

## References

- Ramanathan, V.; Carmichael, G. Global and regional climate changes due to black carbon. *Nat. Geosci.* **2008**, *1*, 221–227. [[CrossRef](#)]
- Seaton, A.; Donaldson, K. Nanoscience, nanotoxicology, and the need to think small. *Lancet* **2005**, *365*, 923–924. [[CrossRef](#)] [[PubMed](#)]
- Cheung, K.; Ntziachristos, L.; Tzankiozis, T.; Schauer, J.; Samaras, Z.; Moore, K.; Sioutas, C. Emissions of particulate trace elements, metals and organic species from gasoline, diesel, and biodiesel passenger vehicles and their relation to oxidative potential. *Aerosol Sci. Technol.* **2010**, *44*, 500–513. [[CrossRef](#)]
- Eckerle, W.A.; Lyford-Pike, E.J.; Stanton, D.W.; LaPointe, L.A.; Whitacre, S.D.; Wall, J.C. Effects of methyl ester biodiesel blends on NOx emissions. *SAE Int. J. Fuels Lubr.* **2009**, *1*, 102–118. [[CrossRef](#)]
- Kim, K.; Kim, D.; Jung, Y.; Bae, C. Spray and combustion characteristics of gasoline and diesel in a direct injection compression ignition engine. *Fuel* **2013**, *109*, 616–626. [[CrossRef](#)]
- Iwabuchi, Y.; Kawai, K.; Shoji, T.; Takeda, Y. *Trial of New Concept Diesel Combustion System-Premixed Compression-Ignited Combustion*; Technical Report, SAE Technical Paper; SAE International: Warrendale, PA, USA, 1999. [[CrossRef](#)]
- Xuan, T.; Pastor, J.V.; García-Oliver, J.M.; García, A.; He, Z.; Wang, Q.; Reyes, M. In-flame soot quantification of diesel sprays under sooting/non-sooting critical conditions in an optical engine. *Appl. Therm. Eng.* **2019**, *149*, 1–10. [[CrossRef](#)]
- Labeckas, G.; Slavinskas, S.; Mažeika, M. The effect of ethanol–diesel–biodiesel blends on combustion, performance and emissions of a direct injection diesel engine. *Energy Convers. Manag.* **2014**, *79*, 698–720. [[CrossRef](#)]
- Heywood, J.B. *Internal Combustion Engine Fundamentals*; McGraw-Hill Education: New York, NY, USA, 2018.
- Flynn, P.F.; Durrett, R.P.; Hunter, G.L.; zur Loye, A.O.; Akinyemi, O.C.; Dec, J.E.; Westbrook, C.K. Diesel combustion: An integrated view combining laser diagnostics, chemical kinetics, and empirical validation. *SAE Trans.* **1999**, *108*, 587–600.
- Siebers, D. Liquid-phase fuel penetration in diesel sprays. *SAE Trans.* **1998**, *107*, 1205–1227.
- Li, D.; He, Z.; Xuan, T.; Zhong, W.; Cao, J.; Wang, Q.; Wang, P. Simultaneous capture of liquid length of spray and flame lift-off length for second-generation biodiesel/diesel blended fuel in a constant volume combustion chamber. *Fuel* **2017**, *189*, 260–269. [[CrossRef](#)]
- Kook, S.; Pickett, L.M. Liquid length and vapor penetration of conventional, Fischer–Tropsch, coal-derived, and surrogate fuel sprays at high-temperature and high-pressure ambient conditions. *Fuel* **2012**, *93*, 539–548. [[CrossRef](#)]
- Siebers, D.; Higgins, B. Flame lift-off on direct-injection diesel sprays under quiescent conditions. *SAE Trans.* **2001**, *110*, 400–421.
- Siebers, D.; Higgins, B.; Pickett, L. Flame lift-off on direct-injection diesel fuel jets: Oxygen concentration effects. *SAE Trans.* **2002**, *111*, 1490–1509.

16. Musculus, M.P.; Dec, J.E.; Tree, D.R. Effects of fuel parameters and diffusion flame lift-off on soot formation in a heavy-duty DI diesel engine. *SAE Trans.* **2002**, *111*, 1467–1489.
17. Nishida, K.; Zhu, J.; Leng, X.; He, Z. Effects of micro-hole nozzle and ultra-high injection pressure on air entrainment, liquid penetration, flame lift-off and soot formation of diesel spray flame. *Int. J. Engine Res.* **2017**, *18*, 51–65. [[CrossRef](#)]
18. Hespel, C.; Houidi, M.B.; Ajrouche, H.; Foucher, F.; Haidous, Y.; Moreau, B.; Nilaphai, O.; Rousselle, C.; Bellenoue, M.; Claverie, A.; et al. Characterization of the ECN spray A in different facilities. Part 2: Spray vaporization and combustion. *Oil Gas Sci. Technol.—Rev. d'IFP Energies Nouv.* **2020**, *75*, 78. [[CrossRef](#)]
19. Naber, J.D.; Siebers, D.L. Effects of gas density and vaporization on penetration and dispersion of diesel sprays. *SAE Trans.* **1996**, *105*, 82–111.
20. Desantes, J.; Payri, R.; Salvador, F.; Soare, V. *Study of the Influence of Geometrical and Injection Parameters on Diesel Sprays Characteristics in Isothermal Conditions*; Technical Report, SAE Technical Paper; SAE International: Warrendale, PA, USA, 2005. [[CrossRef](#)]
21. Payri, R.; Salvador, F.; Gimeno, J.; Zapata, L. Diesel nozzle geometry influence on spray liquid-phase fuel penetration in evaporative conditions. *Fuel* **2008**, *87*, 1165–1176. [[CrossRef](#)]
22. Payri, R.; Salvador, F.; Gimeno, J.; De la Morena, J. Macroscopic behavior of diesel sprays in the near-nozzle field. *SAE Int. J. Engines* **2009**, *1*, 528–536. [[CrossRef](#)]
23. Xu, M.; Sun, Y.; Cui, Y.; Deng, K.; Shi, L. One-dimensional model on fuel penetration in diesel sprays with gas flow. *Int. J. Automot. Technol.* **2016**, *17*, 109–118. [[CrossRef](#)]
24. García-Oliver, J.M.; Margot, X.; Chávez, M.; Karlsson, A. A combined 1D3D-CFD approach for reducing mesh dependency in Diesel spray calculations. *Math. Comput. Model.* **2011**, *54*, 1732–1737. [[CrossRef](#)]
25. Desantes, J.; Margot, X.; Pastor, J.; Chavez, M.; Pinzello, A. CFD- Phenomenological Diesel Spray Analysis under Evaporative Conditions. *Energy Fuels* **2009**, *23*, 3919–3929. [[CrossRef](#)]
26. Campbell, J.; Gosman, A.; Hardy, G. Analysis of premix flame and lift-off in diesel spray combustion using multi-dimensional CFD. *SAE Int. J. Engines* **2009**, *1*, 571–590. [[CrossRef](#)]
27. Taskiran, O.O.; Ergeneman, M. Effect of nozzle dimensions and fuel type on flame lift-off length. *Fuel* **2014**, *115*, 833–840. [[CrossRef](#)]
28. Wiesmann, F.; Strauß, L.; Rieß, S.; Manin, J.; Wan, K.; Lauer, T. Numerical and Experimental Investigations on the Ignition Behavior of OME. *Energies* **2022**, *15*, 6855. [[CrossRef](#)]
29. Payri, R.; Novella, R.; Carreres, M.; Belmar-Gil, M. Modeling gaseous non-reactive flow in a lean direct injection gas turbine combustor through an advanced mesh control strategy. *Proc. Inst. Mech. Eng. Part G J. Aerosp. Eng.* **2020**, *234*, 1788–1810. [[CrossRef](#)]
30. Corral-Gómez, L.; Armas, O.; Soriano, J.A.; Pastor, J.V.; García-Oliver, J.M.; Micó, C. An Optical Engine Used as a Physical Model for Studies of the Combustion Process Applying a Two-Color Pyrometry Technique. *Energies* **2022**, *15*, 4717. [[CrossRef](#)]
31. Settles, G.S. *Schlieren and Shadowgraph Techniques: Visualizing Phenomena in Transparent Media*; Springer Science & Business Media: Berlin/Heidelberg, Germany, 2001.
32. Ma, Y.; Huang, S.; Huang, R.; Zhang, Y.; Xu, S. Spray and evaporation characteristics of n-pentanol–diesel blends in a constant volume chamber. *Energy Convers. Manag.* **2016**, *130*, 240–251. [[CrossRef](#)]
33. Corral-Gómez, L.; Castillo-García, F.J.; Soriano, J.A.; Armas, O. Macroscopic Parameters of Fuel Sprays Injected in an Optical Reciprocating Single-Cylinder Engine: An Approximation by Means of Visualization with Schlieren Technique. *Sensors* **2023**, *23*, 6747. [[CrossRef](#)]
34. Tuncer, C. *Analysis of Turbulent Flows*; Elsevier: Amsterdam, The Netherlands, 2004.
35. Martos, F.J.; Soriano, J.A.; Braic, A.; Fernández-Yáñez, P.; Armas, O. A CFD Modelling Approach for the Operation Analysis of an Exhaust Backpressure Valve Used in a Euro 6 Diesel Engine. *Energies* **2023**, *16*, 4112. [[CrossRef](#)]
36. Martos, F.J.; Soriano, J.A.; Mata, C.; Armas, O.; Soto, F. Impact of alternative and fossil diesel fuels on internal flow of injection nozzle. *Int. J. Engine Res.* **2022**, *23*, 940–957. [[CrossRef](#)]
37. Safarov, J.; Ashurova, U.; Ahmadov, B.; Hassel, E. Vapor pressure of 1-butanol and Diesel B0 binary fuel blends. *J. Serbian Chem. Soc.* **2019**, *84*, 599–607. [[CrossRef](#)]
38. Armas, O.; Martínez-Martínez, S.; Mata, C.; Pacheco, C. Alternative method for bulk modulus estimation of Diesel fuels. *Fuel* **2016**, *167*, 199–207. [[CrossRef](#)]
39. Cristofaro, M.; Edelbauer, W.; Koukouvinis, P.; Gavaises, M. A numerical study on the effect of cavitation erosion in a diesel injector. *Appl. Math. Model.* **2020**, *78*, 200–216. [[CrossRef](#)]
40. Salvador, F.J.; De la Morena, J.; Bracho, G.; Jaramillo, D. Computational investigation of diesel nozzle internal flow during the complete injection event. *J. Braz. Soc. Mech. Sci. Eng.* **2018**, *40*, 153. [[CrossRef](#)]
41. Miller, R.; Harstad, K.; Bellan, J. Evaluation of equilibrium and non-equilibrium evaporation models for many-droplet gas-liquid flow simulations. *Int. J. Multiph. Flow* **1998**, *24*, 1025–1055. [[CrossRef](#)]
42. Sazhin, S.S. Advanced models of fuel droplet heating and evaporation. *Prog. Energy Combust. Sci.* **2006**, *32*, 162–214. [[CrossRef](#)]
43. Ranz, W.E. Evaporation from Drops-I and-II. *Chem. Eng. Prog.* **1952**, *48*, 141–146.
44. O'Rourke, P.J. Collective Drop Effects on Vaporizing Liquid Sprays. Ph.D. Thesis, Princeton University, Princeton, NJ, USA, 1981.
45. Hossainpour, S.; Binesh, A. Investigation of fuel spray atomization in a DI heavy-duty diesel engine and comparison of various spray breakup models. *Fuel* **2009**, *88*, 799–805. [[CrossRef](#)]

46. Reitz, R.D. Modeling atomization processes in high-pressure vaporizing sprays. *At. Spray Technol.* **1987**, *3*, 309–337.
47. Xin, J.; Ricart, L.; Reitz, R. Computer modeling of diesel spray atomization and combustion. *Combust. Sci. Technol.* **1998**, *137*, 171–194. [[CrossRef](#)]
48. Liu, A.B.; Mather, D.; Reitz, R.D. Modeling the effects of drop drag and breakup on fuel sprays. *SAE Trans.* **1993**, *102*, 83–95. [[CrossRef](#)]
49. Beale, J.C.; Reitz, R.D. Modeling spray atomization with the Kelvin-Helmholtz/Rayleigh-Taylor hybrid model. *At. Sprays* **1999**, *9*. [[CrossRef](#)]
50. Patterson, M.A.; Reitz, R.D. Modeling the effects of fuel spray characteristics on diesel engine combustion and emission. *SAE Trans.* **1998**, *107*, 27–43. [[CrossRef](#)]
51. Desantes, J.M.; Payri, R.; Salvador, F.J.; Gil, A. Development and validation of a theoretical model for diesel spray penetration. *Fuel* **2006**, *85*, 910–917. [[CrossRef](#)]
52. Pastor, J.V.; García-Oliver, J.M.; Micó, C.; García-Carrero, A.A.; Gómez, A. Experimental study of the effect of hydrotreated vegetable oil and oxymethylene ethers on main spray and combustion characteristics under engine combustion network spray a conditions. *Appl. Sci.* **2020**, *10*, 5460. [[CrossRef](#)]

**Disclaimer/Publisher’s Note:** The statements, opinions and data contained in all publications are solely those of the individual author(s) and contributor(s) and not of MDPI and/or the editor(s). MDPI and/or the editor(s) disclaim responsibility for any injury to people or property resulting from any ideas, methods, instructions or products referred to in the content.